

# EFFICIENT UNCERTAINTY QUANTIFICATION IN UNSTEADY AEROELASTIC SIMULATIONS

Jeroen A.S. Witteveen<sup>1</sup> and Hester Bijl<sup>1</sup>

<sup>1</sup>Delft University of Technology  
Kluyverweg 1, 2629HS, Delft  
j.a.s.witteveen@tudelft.nl

**Keywords.** Uncertainty quantification, stochastic collocation, unsteady, aeroelasticity.

**Abstract.** An efficient uncertainty quantification method for unsteady problems is presented in order to achieve a constant accuracy in time for a constant number of samples. The approach is applied to the aeroelastic problems of a transonic airfoil flutter system and the AGARD 445.6 wing benchmark with uncertainties in the flow and the structure.

## 1 INTRODUCTION

Numerical errors in multi-physics simulations start to reach acceptable engineering accuracy levels due to the increasing availability of computational resources. Nowadays, uncertainties in modeling multi-scale phenomena in fluid-structure, fluid-thermal, and aero-acoustic interactions have a larger effect on the accuracy of computational predictions than discretization errors. It is therefore especially important in multi-physics applications to systematically quantify the effect of physical variations on a routine basis. Furthermore, unsteady fluid-structure interaction applications are practical aeronautical examples of dynamical systems which are known to amplify initial variations with time. In these problems, natural irreducible input variability can trigger the earlier onset of unstable flutter behavior, which can lead to unexpected fatigue damage and structural failure.

Polynomial Chaos uncertainty quantification methods [1–10] however usually result in a fast increasing number of samples with time to resolve the effect of random parameters in dynamical systems with a constant accuracy [11]. Resolving the asymptotic stochastic effect, which is of practical interest in post-flutter analysis, can in these long time integration problems lead to thousands of required samples. The increasing number of samples is caused by the increasing nonlinearity of the response surface for increasing integration times. This effect is especially profound in problems with oscillatory solutions in which the frequency of the response is affected by the random parameters. The frequency differences between the realizations lead to increasing phase differences with time, which in turn result in an increasingly oscillatory response surface and more required samples.

In order to enable efficient uncertainty quantification in time-dependent simulations, a special uncertainty quantification methodology for unsteady oscillatory problems is developed. The approach based on time-independent parameterization of oscillatory samples achieves a constant uncertainty quantification interpolation accuracy in time with a constant number of samples [12]. A parameterization in terms of the time-independent functionals frequency, relative phase, amplitude, a reference value, and the normalized period shape is used for period-1 responses. The extension with a damping factor and an algorithm for identifying higher-period shape functions is also applicable to more complex and non-periodic realizations [13].

A second uncertainty quantification formulation for achieving a constant accuracy in time with a constant number of samples is developed based on interpolation of oscillatory samples at constant phase instead of at constant time [14]. The scaling of the samples with their phase eliminates the effect of the increasing phase differences in the response, which usually leads to the fast increasing number of samples with time. The resulting formulation is not subject to a parameterization error and it can resolve time-dependent functionals that occur for example in transient behavior. It is also proven that phase-scaled uncertainty quantification results in a bounded error as function of the phase for periodic responses and under certain conditions also in a bounded error in time [15]. The unsteady approaches are independent of the employed non-intrusive uncertainty quantification to perform the actual interpolation of the oscillatory samples. Here the Simplex Elements Polynomial Chaos (SEPC) method based on Newton-Cotes quadrature in simplex elements is employed [16]. Since the piecewise polynomial approximation of the response of SEPC satisfies the extrema diminishing robustness criterion extended to probability space, it enables us to resolve also bifurcation phenomena reliably [15]. The formulation is also extended to multi-frequency responses of continuous structures by using a wavelet decomposition preprocessing step in order to treat the different frequency components separately [17].

After the introduction of the mathematical statement of the uncertainty quantification problem in section 2, the efficient uncertainty quantification method for unsteady problems is presented in section 3. The developed approach is applied to the unsteady fluid-structure interaction test cases of a two-dimensional airfoil flutter problem and the three-dimensional aeroelastic AGARD 445.6 wing. In section 4 the stochastic post-flutter analysis of a two-degree-of-freedom rigid airfoil in Euler flow with nonlinear structural stiffness in pitch and plunge with uncertainty in a combination of randomness in two system parameters is considered. The effect of free stream velocity fluctuation is analyzed in section 5 for the AGARD aeroelastic wing in the transonic flow regime 5% below the deterministic flutter speed. Additional applications to other aeroelastic systems are reported in [18–20]. Finally, the conclusions are summarized in section 6.

## 2 MATHEMATICAL FORMULATION OF THE UNCERTAINTY QUANTIFICATION PROBLEM

Consider a dynamical system subject to  $n_a$  uncorrelated second-order random input parameters  $\mathbf{a}(\omega) = \{a_1(\omega), \dots, a_{n_a}(\omega)\} \in A$  with parameter space  $A \in \mathbb{R}^{n_a}$ , which governs an oscillatory response  $u(\mathbf{x}, t, \mathbf{a})$

$$\mathcal{L}(\mathbf{x}, t, \mathbf{a}; u(\mathbf{x}, t, \mathbf{a})) = S(\mathbf{x}, t, \mathbf{a}), \quad (1)$$

with operator  $\mathcal{L}$  and source term  $S$  defined on domain  $D \times T \times A$ , and appropriate initial and boundary conditions. The spatial and temporal dimensions are defined as  $\mathbf{x} \in D$  and  $t \in T$ , respectively, with  $D \subset \mathbb{R}^d$ ,  $d = \{1, 2, 3\}$ , and  $T = [0, t_{\max}]$ . A realization of the set of outcomes  $\Omega$  of the probability space  $(\Omega, \mathcal{F}, P)$  is denoted by  $\omega \in \Omega = [0, 1]^{n_a}$ , with  $\mathcal{F} \subset 2^\Omega$  the  $\sigma$ -algebra of events and  $P$  a probability measure.

Here we consider a non-intrusive uncertainty quantification method  $l$  which constructs a weighted approximation  $w(\mathbf{x}, t, \mathbf{a})$  of response surface  $u(\mathbf{x}, t, \mathbf{a})$  based on  $n_s$  deterministic solutions  $v_k(\mathbf{x}, t) \equiv u(\mathbf{x}, t, \mathbf{a}_k)$  of (1) for different parameter values  $\mathbf{a}_k \equiv \mathbf{a}(\omega_k)$  for  $k =$

1, ...,  $n_s$ . The samples  $v_k(\mathbf{x}, t)$  can be obtained by solving the deterministic problem

$$\mathcal{L}(\mathbf{x}, t, \mathbf{a}_k; v_k(\mathbf{x}, t)) = \mathcal{S}(\mathbf{x}, t, \mathbf{a}_k), \quad (2)$$

for  $k = 1, \dots, n_s$ , using standard spatial discretization methods and time marching schemes. A non-intrusive uncertainty quantification method  $l$  is then a combination of a sampling method  $g$  and an interpolation method  $h$ . Sampling method  $g$  defines the  $n_s$  sampling points  $\{\mathbf{a}_k\}_{k=1}^{n_s}$  and returns the deterministic samples  $\mathbf{v}(\mathbf{x}, t) = \{v_1(\mathbf{x}, t), \dots, v_{n_s}(\mathbf{x}, t)\}$ . Interpolation method  $h$  constructs an interpolation surface  $w(\mathbf{x}, t, \mathbf{a})$  through the  $n_s$  samples  $\mathbf{v}(\mathbf{x}, t)$  as an approximation of  $u(\mathbf{x}, t, \mathbf{a})$ . We are eventually interested in an approximation of the probability distribution and statistical moments  $\mu_{u_i}(\mathbf{x}, t)$  of the output  $u(\mathbf{x}, t, \mathbf{a})$ , which can be obtained by sorting and weighted integration of  $w(\mathbf{x}, t, \mathbf{a})$

$$\mu_{u_i}(\mathbf{x}, t) \approx \mu_{w_i}(\mathbf{x}, t) = \int_A w(\mathbf{x}, t, \mathbf{a})^i f_{\mathbf{a}}(\mathbf{a}) d\mathbf{a}. \quad (3)$$

This information can be used for reducing design safety factors and robust design optimization, in contrast to reliability analysis in which the probability of failure is determined [21].

### 3 AN EFFICIENT UNCERTAINTY QUANTIFICATION METHOD FOR UNSTEADY PROBLEMS

The efficient uncertainty quantification formulation for oscillatory responses based on interpolation of scaled samples at constant phase is developed in section 3.2. The robust extrema diminishing uncertainty quantification method based on Newton-Cotes quadrature in simplex elements employed in the unsteady approach is first presented in the next section.

#### 3.1 Robust extrema diminishing uncertainty quantification

A multi-element uncertainty quantification method  $l$  evaluates integral (3) by dividing parameter space  $A$  into  $n_e$  non-overlapping simplex elements  $A_j \subset A$

$$\mu_{w_i}(\mathbf{x}, t) = \sum_{j=1}^{n_e} \int_{A_j} w(\mathbf{x}, t, \mathbf{a})^i f_{\mathbf{a}}(\mathbf{a}) d\mathbf{a}. \quad (4)$$

Here we consider a multi-element Polynomial Chaos method based on Newton-Cotes quadrature points and simplex elements [16]. A piecewise polynomial approximation  $w(\mathbf{x}, t, \mathbf{a})$  is then constructed based on  $n_s$  deterministic solutions  $v_{j,k}(\mathbf{x}, t) = u(\mathbf{x}, t, \mathbf{a}_{j,k})$  for the values of the random parameters  $\mathbf{a}_{j,k}$  that correspond to the  $\tilde{n}_s$  Newton-Cotes quadrature points of degree  $d$  in the elements  $A_j$

$$\mu_{w_i}(\mathbf{x}, t) = \sum_{j=1}^{n_e} \sum_{k=1}^{\tilde{n}_s} c_{j,k} v_{j,k}(\mathbf{x}, t)^i, \quad (5)$$

where  $c_{j,k}$  is the weighted integral of the Lagrange interpolation polynomial  $L_{j,k}(\mathbf{a})$  through Newton-Cotes quadrature point  $k$  in element  $A_j$

$$c_{j,k} = \int_{A_j} L_{j,k}(\mathbf{a}) f_{\mathbf{a}}(\mathbf{a}) d\mathbf{a}, \quad (6)$$

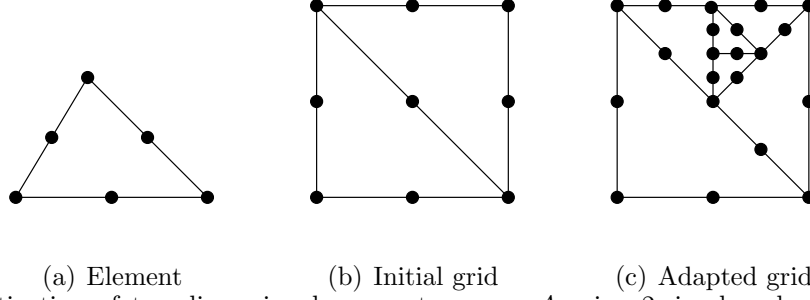


Figure 1: Discretization of two-dimensional parameter space  $A$  using 2-simplex elements and second-degree Newton-Cotes quadrature points given by the dots.

for  $j = 1, \dots, n_e$  and  $k = 1, \dots, \tilde{n}_s$ . Here, second degree Newton-Cotes quadrature with  $d = 2$  is considered in combination with adaptive mesh refinement in probability space, since low order approximations are more effective for approximating response surfaces with singularities. The initial discretization of parameter space  $A$  for the adaptive scheme consists of the minimum of  $n_{e_{ini}} = n_a!$  simplex elements and  $n_{s_{ini}} = 3^{n_a}$  samples, see Figure 1. The example of Figure 1 for two random input parameters can geometrically be extended to higher dimensional probability spaces. The elements  $A_j$  are adaptively refined using a refinement measure  $\rho_j$  based on the largest absolute eigenvalue of the Hessian  $H_j$ , as measure of the curvature of the response surface approximation in the elements, weighted by the probability  $f_j$  contained by the elements

$$f_j = \int_{A_j} f_{\mathbf{a}}(\mathbf{a}) d\mathbf{a}, \quad (7)$$

with  $\sum_{j=1}^{n_e} f_j = 1$ . The stochastic grid refinement is terminated when convergence measure  $\delta_{n_e}$  is smaller than a threshold value  $\delta_{n_e} < \bar{\delta}$  where

$$\delta_{n_e} = \max \left( \frac{\| \mu_{w_{\lfloor n_e/2 \rfloor}}(\mathbf{x}, t) - \mu_{w_{n_e}}(\mathbf{x}, t) \|_{\infty}}{\| \mu_{w_{n_e}}(\mathbf{x}, t) \|_{\infty}}, \frac{\| \sigma_{w_{\lfloor n_e/2 \rfloor}}(\mathbf{x}, t) - \sigma_{w_{n_e}}(\mathbf{x}, t) \|_{\infty}}{\| \sigma_{w_{n_e}}(\mathbf{x}, t) \|_{\infty}} \right), \quad (8)$$

with  $\mu_w(\mathbf{x}, t)$  and  $\sigma_w(\mathbf{x}, t)$  the mean and standard deviation of  $w(\mathbf{x}, t, \omega)$ , or when a maximum number of samples  $\tilde{n}_s$  is reached. Convergence measure  $\delta_{n_e}$  can be extended to include also higher statistical moments of the output.

In elements where the quadratic second degree interpolation results in an extremum other than in a quadrature point, the element is subdivided into  $\tilde{n}_e = 2^{n_a}$  subelements with a linear first degree Newton-Cotes approximation of the response without performing additional deterministic solves. It is proven in [15] that the resulting approach satisfies the extrema diminishing (ED) robustness concept in probability space

$$\min_A(w(\mathbf{a})) \geq \min_A(u(\mathbf{a})) \wedge \max_A(w(\mathbf{a})) \leq \max_A(u(\mathbf{a})) \quad \forall u(\mathbf{a}), \quad (9)$$

where the arguments  $\mathbf{x}$  and  $t$  are omitted for simplicity of the notation. The ED property leads to the advantage that no non-zero probabilities of unphysical realizations can be predicted due to overshoots or undershoots at discontinuities in the response. Due to the location of the Newton-Cotes quadrature points the deterministic samples are also reused in successive refinements and the samples are used in approximating the response in multiple elements.

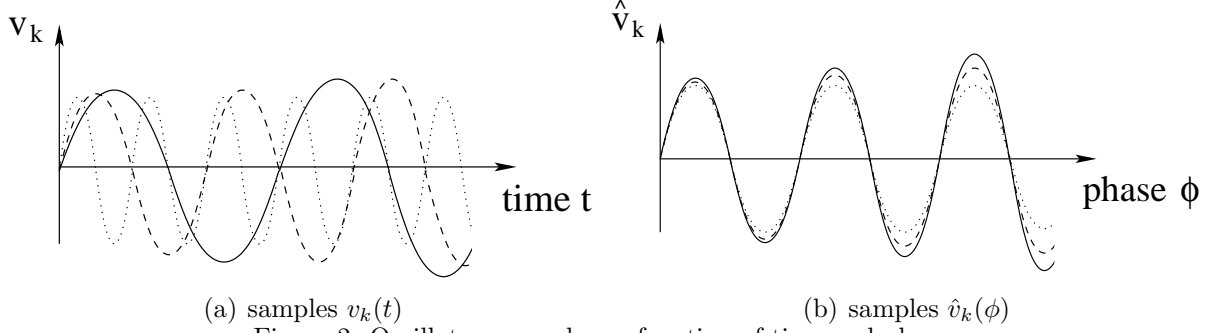


Figure 2: Oscillatory samples as function of time and phase.

### 3.2 Efficient uncertainty quantification interpolation at constant phase

Polynomial Chaos methods usually require a fast increasing number of samples with time to maintain a constant accuracy. Performing the uncertainty quantification interpolation of oscillatory samples at constant phase instead of at constant time results, however, in a constant accuracy with a constant number of samples. Assume, therefore, that solving equation (2) for realizations of the random parameters  $\mathbf{a}_k$  results in oscillatory samples  $v_k(t) = u(\mathbf{a}_k)$ , of which the phase  $v_{\phi_k}(t) = \phi(t, \mathbf{a}_k)$  is a well-defined monotonically increasing function of time  $t$  for  $k = 1, \dots, n_s$ .

In order to interpolate the samples  $\mathbf{v}(t) = \{v_1(t), \dots, v_{n_a}(t)\}$  at constant phase, first, their phase as function of time  $\mathbf{v}_\phi(t) = \{v_{\phi_1}(t), \dots, v_{\phi_{n_a}}(t)\}$  is extracted from the deterministic solves  $\mathbf{v}(t)$ . Second, the time series for the phase  $\mathbf{v}_\phi(t)$  are used to transform the samples  $\mathbf{v}(t)$  into functions of their phase  $\hat{\mathbf{v}}(\mathbf{v}_\phi(t))$  according to

$$\hat{v}_k(v_{\phi_k}(t)) = v_k(t), \quad (10)$$

for  $k = 1, \dots, n_s$ , see Figure 2. And, third, the sampled phases  $\mathbf{v}_\phi(t)$  are interpolated to the function  $w_\phi(t, \mathbf{a})$

$$w_\phi(t, \mathbf{a}) = h(\mathbf{v}_\phi(t)), \quad (11)$$

as approximation of  $\phi(t, \mathbf{a})$ . Finally, the transformed samples  $\hat{\mathbf{v}}(\mathbf{v}_\phi(t))$  are interpolated at a constant phase  $\varphi \in w_\phi(t, \mathbf{a})$  to

$$\hat{w}(\varphi, \mathbf{a}) = h(\hat{\mathbf{v}}(\varphi)). \quad (12)$$

Repeating the latter interpolation for all phases  $\varphi \in w_\phi(t, \mathbf{a})$  results in the function  $\hat{w}(w_\phi(t, \mathbf{a}), \mathbf{a})$ . The interpolation  $\hat{w}(w_\phi(t, \mathbf{a}), \mathbf{a})$  is then transformed back to an approximation in the time domain  $w(t, \mathbf{a})$  as follows

$$w(t, \mathbf{a}) = \hat{w}(w_\phi(t, \mathbf{a}), \mathbf{a}). \quad (13)$$

The resulting function  $w(t, \mathbf{a})$  is an approximation of the unknown response surface  $u(t, \mathbf{a})$  as function of time  $t$  and the random parameters  $\mathbf{a}(\omega)$ . The actual sampling  $g$  and interpolation  $h$  is performed using the extrema diminishing uncertainty quantification method  $l$  based on Newton-Cotes quadrature in simplex elements described in the previous section.

This uncertainty quantification formulation for oscillatory responses is proven to achieve a bounded error  $\hat{\varepsilon}(\varphi, \mathbf{a}) = |\hat{w}(\varphi, \mathbf{a}) - \hat{u}(\varphi, \mathbf{a})|$  as function of phase  $\varphi$  for periodic responses according to

$$\hat{\varepsilon}(\varphi, \mathbf{a}) < \delta \quad \forall \varphi \in \mathbb{R}, \mathbf{a} \in A, \quad (14)$$

where  $\delta$  is defined by

$$\hat{\varepsilon}(\varphi, \mathbf{a}) < \delta, \quad \forall \varphi \in [0, 1], \mathbf{a} \in A. \quad (15)$$

The error  $\varepsilon(t, \mathbf{a}) = |w(t, \mathbf{a}) - u(t, \mathbf{a})|$  is also bounded in time under certain conditions, see [15].

The phases  $\mathbf{v}_\phi(t)$  are extracted from the samples based on the local extrema of the time series  $\mathbf{v}(t)$ . A trial and error procedure identifies a cycle of oscillation based on two or more successive local maxima. The selected cycle is accepted if the maximal error of its extrapolation in time with respect to the actual sample is smaller than a threshold value  $\bar{\varepsilon}_k$  for at least one additional cycle length. The functions for the phases  $\mathbf{v}_\phi(t)$  in the whole time domain  $T$  are constructed by identifying all successive cycles of  $\mathbf{v}(t)$  and linear extrapolation to  $t = 0$  and  $t = t_{\max}$  before and after the first and last complete cycle, respectively. The phase is normalized to zero at the start of the first cycle and a user defined parameter determines whether the sample is assumed to attain a local extremum at  $t = 0$ . The interpolation at constant phase is restricted to the time domain that corresponds to the range of phases that is reached by all samples in each of the elements. If the phase  $v_{\phi_k}(t)$  cannot be extracted from one of the samples  $v_k(t)$  for  $k = 1, \dots, n_s$ , then uncertainty quantification interpolation  $h$  is directly applied to the time-dependent samples  $\mathbf{v}(t)$ .

#### 4 TRANSONIC AIRFOIL FLUTTER

The combined effect of independent randomness in the ratio of natural frequencies  $\bar{\omega}(\omega)$  and the free stream velocity  $U_\infty(\omega)$  on the post-flutter behavior of an elastically mounted airfoil is analyzed. The structural model of the pitch-plunge airfoil with cubic nonlinear spring stiffness is given by [22, 23]:

$$\xi'' + x_\alpha \alpha'' + \left(\frac{\bar{\omega}}{U^*}\right)^2 (\xi + \beta_\xi \xi^3) = -\frac{1}{\pi\mu} C_1(\tau), \quad (16)$$

$$\frac{x_\alpha}{r_\alpha^2} \xi'' + \alpha'' + \frac{1}{U^{*2}} (\alpha + \beta_\alpha \alpha^3) = \frac{2}{\pi\mu r_\alpha^2} C_m(\tau), \quad (17)$$

where  $\beta_\xi = 0\text{m}^{-2}$  and  $\beta_\alpha = 300\text{rad}^{-2}$  are the cubic spring parameters,  $\xi(\tau) = h/b$  is the non-dimensional plunge displacement of the elastic axis, see Figure 3,  $\alpha(\tau)$  is the pitch angle, and  $(\cdot)$  denotes differentiation with respect to non-dimensional time  $\tau = Ut/b$ , with half-chord length  $b = c/2 = 0.5\text{m}$ . The radius of gyration around the elastic axis is  $r_\alpha b = 0.25\text{m}$ , bifurcation parameter  $U^*$  is defined as  $U^* = U/(b\omega_\alpha)$ , and the airfoil-air mass ratio is  $\mu = m/\pi\rho_\infty b^2 = 100$ , with  $m$  the airfoil mass. The elastic axis is located at a distance  $a_h b = -0.25\text{m}$  from the mid-chord position and the mass center is located at a distance  $x_\alpha b = 0.125\text{m}$  from the elastic axis. The ratio of natural frequencies is defined as  $\bar{\omega}(\omega) = \omega_\xi/\omega_\alpha$ , with  $\omega_\xi$  and  $\omega_\alpha$  the natural frequencies of the airfoil in pitch and plunge, respectively. The randomness in  $\bar{\omega}(\omega)$  is described by a uniform distribution around mean value  $\mu_{\bar{\omega}} = 0.25$  with a coefficient of variation of 10%. The free stream velocity  $U_\infty(\omega)$  is subject to a symmetric unimodal beta distribution with  $\beta_1 = \beta_2 = 2$  with a coefficient of variation of 1% around mean  $\mu_{U_\infty} = 276.27\text{m/s}$ , which corresponds to  $M_\infty = 0.8$ .

The non-dimensional aerodynamic lift and moment coefficients,  $C_1(\tau)$  and  $C_m(\tau)$ , are determined by solving the unsteady Euler equations. The two-dimensional flow domain is discretized by an unstructured hexahedral mesh of  $12 \cdot 10^3$  cells, which was selected based

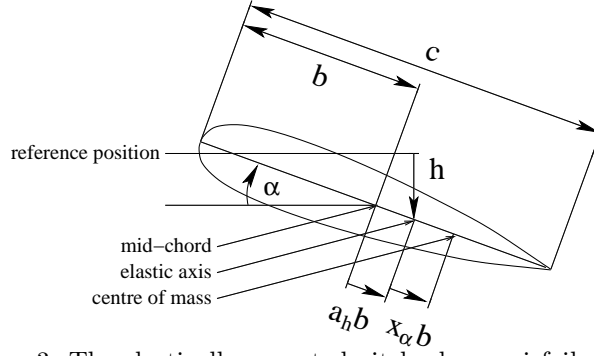


Figure 3: The elastically mounted pitch-plunge airfoil model.

on a grid convergence study. The governing equations are discretized using a second order central finite volume discretization stabilized with artificial dissipation. An Arbitrary Lagrangian-Eulerian formulation is employed to couple the fluid mesh with the movement of the structure. The fluid mesh is deformed using radial basis function interpolation of the boundary displacements [24]. Time integration is performed using the second order BDF-2 method until  $t = 3$  with time step  $\Delta t = 0.002$ , which was established after a time step refinement study. Initially the airfoil is at rest at a deflection of  $\alpha(0) = 0.1^\circ$  and  $\xi(0) = 0$  from its equilibrium position. In order to study the post-bifurcation behavior, the bifurcation parameter  $U^*$  is fixed at 130% of the deterministic linear bifurcation point for the mean values of the random parameters. The stochastic behavior of the angle of attack  $\alpha(t, \omega)$  is resolved as indicator for the post-flutter airfoil behavior.

The Unsteady Adaptive Stochastic Finite Elements response surface approximation of the angle of attack  $\alpha(t, \omega)$  as function of the random parameters  $\bar{\omega}(\omega)$  and  $U_\infty(\omega)$  at  $t = \{0.5; 1.5; 2.5\}$  given in Figure 4 shows an increasingly oscillatory response surface with time. The 10% variation in  $\bar{\omega}(\omega)$  has a larger effect on the frequency of the response than  $U_\infty(\omega)$  with 1% variation. Both parameters have a small effect on the amplitude of the oscillation of  $\alpha(t, \omega)$  of approximately  $3^\circ$ . At  $t = 0.5$  the airfoil exhibits transient behavior from its initial perturbation of  $\alpha(0) = 0.1^\circ$ , which is indicated by the smaller amplitude of the response surface variations of approximately  $2^\circ$ . These results are obtained using the time-independent grid in probability space shown in Figure 4d with  $n_s = 9$  samples,  $n_e = 2$  elements, and  $n_{e_{\text{sub}}} = 4096$  post-processing subelements.

The resulting UASFE approximation of the mean  $\mu_\alpha(t)$  and standard deviation  $\sigma_\alpha(t)$  of the angle of attack  $\alpha(t, \omega)$  in Figure 5 shows two frequency signals due to the effect of the two random parameters on the frequency of the response. The mean  $\mu_\alpha(t)$  exhibits initially an increasing oscillation caused by the deterministic transient of the samples, after which it develops a decaying oscillation due to the effect of the random parameters on the frequency of the response. The large effect of the random parameters on the dynamical system is illustrated by the fast initial increase of the standard deviation  $\sigma_\alpha(t)$  from its deterministic initial condition. Although the deterministic post-flutter behavior is highly unsteady, the stochastic response reaches a steady asymptotic behavior with a standard deviation of  $\sigma_\alpha = 1.6^\circ$ , which is a factor 16 larger than the initial angle of attack  $\alpha(0) = 0.1^\circ$ . The discretizations with  $n_s = \{9, 13, 25\}$  samples and  $n_e = \{2, 4, 8\}$  uniformly refined elements, respectively, indicate that the results are uniformly converged in time. The approximation with  $n_s = 25$  is converged up to  $\delta_{n_e} = 6.2 \cdot 10^{-3}$ , where  $\delta_{n_e}$  is defined by (8). The local convergence for  $\mu_\alpha(t)$  and  $\sigma_\alpha(t)$  at  $t = \{0.5; 1.0; 1.5; 2.0; 2.5\}$  given in

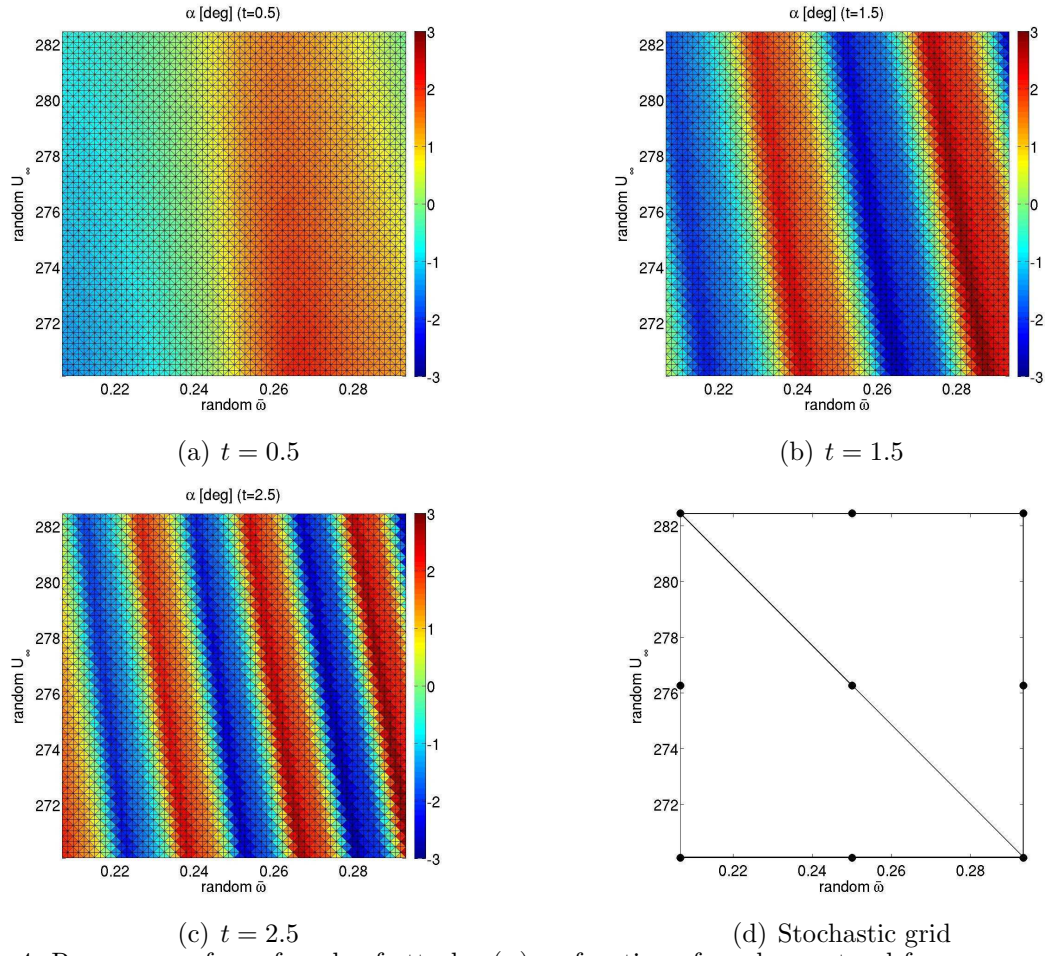


Figure 4: Response surface of angle of attack  $\alpha(\omega)$  as function of random natural frequency ratio  $\bar{\omega}(\omega)$  and free stream velocity  $U_\infty(\omega)$  for transonic airfoil flutter.



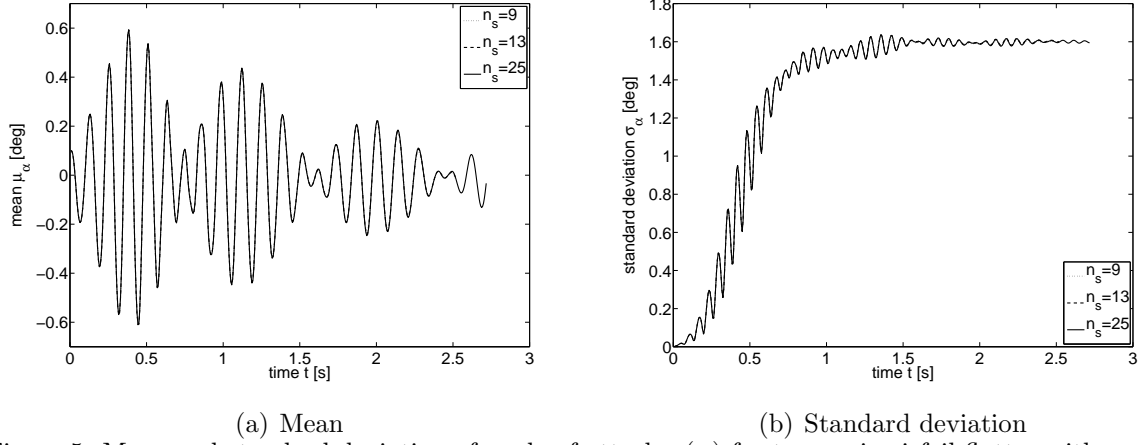


Figure 5: Mean and standard deviation of angle of attack  $\alpha(\omega)$  for transonic airfoil flutter with random natural frequency ratio  $\bar{\omega}(\omega)$  and free stream velocity  $U_\infty(\omega)$ .

Table 1: Convergence measure  $\delta_{n_e}$  for mean angle of attack  $\alpha(t, \omega)$  for transonic airfoil flutter with random natural frequency ratio  $\bar{\omega}(\omega)$  and free stream velocity  $U_\infty(\omega)$ .

$n_s$	$n_e$	$t = 0.5$	$t = 1.0$	$t = 1.5$	$t = 2.0$	$t = 2.5$
13	4	$0.640 \cdot 10^{-3}$	$3.712 \cdot 10^{-3}$	$4.426 \cdot 10^{-3}$	$7.207 \cdot 10^{-3}$	$4.331 \cdot 10^{-3}$
25	8	$0.268 \cdot 10^{-3}$	$2.455 \cdot 10^{-3}$	$3.138 \cdot 10^{-3}$	$4.422 \cdot 10^{-3}$	$2.684 \cdot 10^{-3}$

Tables 1 and 2 for  $n_s = \{13, 25\}$  shows no clear increase of convergence measure  $\delta$  with time. This illustrates that the convergence and the accuracy of the UASFE approximation are in practice constant in time.

## 5 THREE-DIMENSIONAL TRANSONIC WING

The transonic AGARD 445.6 wing [25] is a standard benchmark case for the fluid-structure interaction of a three-dimensional continuous structure. The discretization of the aeroelastic configuration is described in section 5.1. In section 5.2 randomness is introduced in the free stream velocity. The stochastic response of the system and the flutter probability are determined.

### 5.1 AGARD 445.6 wing benchmark problem

The AGARD aeroelastic wing configuration number 3 [25] known as the weakened model is considered here with a NACA 65A004 symmetric airfoil, taper ratio of 0.66,  $45^\circ$  quarter-chord sweep angle, and a 2.5-foot semi-span subject to an inviscid flow. The structure is described by a nodal discretization using an undamped linear finite element model in the *Matlab* finite element toolbox *OpenFEM* [26]. The discretization contains in the chordal and spanwise direction  $6 \times 6$  brick-elements with 20 nodes and 60 degrees-of-freedom,

Table 2: Convergence measure  $\delta_{n_e}$  for the standard deviation of angle of attack  $\alpha(t, \omega)$  for transonic airfoil flutter with random natural frequency ratio  $\bar{\omega}(\omega)$  and free stream velocity  $U_\infty(\omega)$ .

$n_s$	$n_e$	$t = 0.5$	$t = 1.0$	$t = 1.5$	$t = 2.0$	$t = 2.5$
13	4	$2.943 \cdot 10^{-3}$	$3.275 \cdot 10^{-3}$	$7.500 \cdot 10^{-3}$	$5.378 \cdot 10^{-3}$	$3.896 \cdot 10^{-3}$
25	8	$0.973 \cdot 10^{-3}$	$4.388 \cdot 10^{-3}$	$0.859 \cdot 10^{-3}$	$2.194 \cdot 10^{-3}$	$3.344 \cdot 10^{-3}$

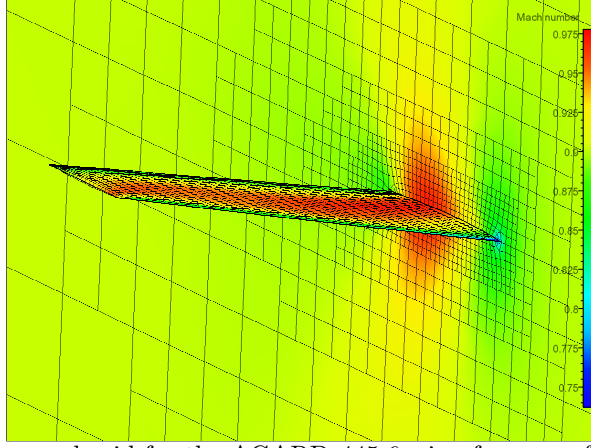


Figure 6: Initial condition and grid for the AGARD 445.6 wing for mean free stream velocity  $\mu_{U_\infty}$ .

and at the leading and trailing edge  $2 \times 6$  pentahedral elements with 15 nodes and 45 degrees-of-freedom as in [27]. The orthotropic material properties are obtained from [28] and the fiber orientation is taken parallel to the quarter-chord line.

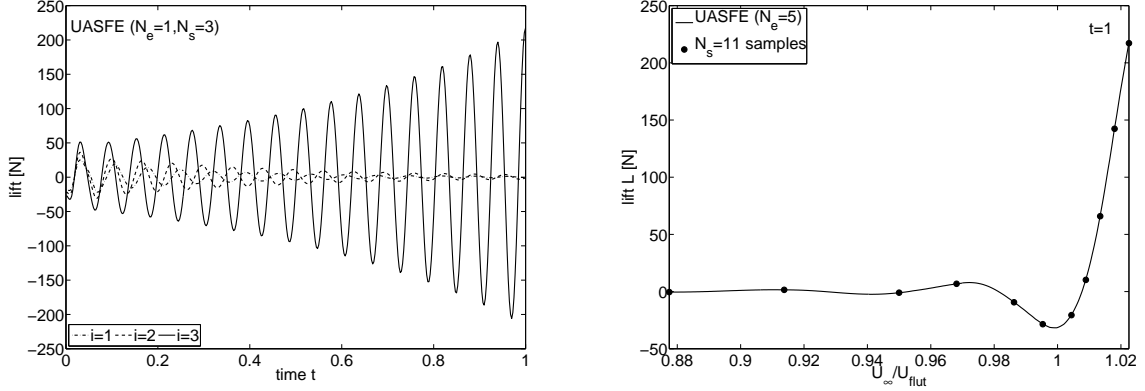
The Euler equations for inviscid flow [29] are solved using a second-order central finite volume discretization on a  $60 \times 15 \times 30$ m domain using an unstructured hexahedral mesh. The free stream conditions for the density  $\rho_\infty = 0.099468 \text{ kg/m}^3$  and pressure  $p_\infty = 7704.05 \text{ Pa}$  are taken from [25]. Time integration of the samples is performed using a third-order implicit Runge-Kutta scheme [30] until  $t = 1.25 \text{ s}$  to determine the stochastic solution until  $t = 1 \text{ s}$ . The first bending mode with a vertical tip displacement of  $y_{\text{tip}} = 0.01 \text{ m}$  is used as initial condition for the structure, see Figure 6.

The coupled fluid-structure interaction system is solved using a partitioned IMEX scheme [31,32] with explicit treatment of the coupling terms without sub-iterations. An Arbitrary Lagrangian-Eulerian formulation is employed to couple the fluid mesh with the movement of the structure. The flow forces and the structural displacements are imposed on the structure and the flow using nearest neighbor and radial basis function interpolation [27], respectively. The fluid mesh is also deformed using radial basis function interpolation of the boundary displacements [24]. A convergence study has been performed to determine a suitable flow mesh discretization and time step size. Deterministic results for the selected flow mesh with  $3.1 \cdot 10^4$  volumes and time step of  $\Delta t = 2.5 \cdot 10^{-3} \text{ s}$  agree well with experimental and computational results in the literature [25,27,33]. The deterministic flutter velocity is found to be  $U_{\text{flut}} = 313 \text{ m/s}$ , which corresponds to a Mach number of  $M_\infty = 0.951$ .

## 5.2 Randomness causes non-zero flutter probability

In the following, the effect of randomness in the free stream velocity  $U_\infty(\omega)$  is studied. The mean free stream velocity is chosen 5% below the actual deterministic flutter velocity,  $\mu_{U_\infty} = 0.95 U_{\text{flut}}$ , to assess the effectiveness of a realistic design safety factor. The coefficient of variation of the assumed unimodal beta distribution is set to  $\text{cv}_{U_\infty} = 3.5\%$ . The outputs of interest are the lift  $L(t, \omega)$  and the vertical tip displacement of the tip-node  $y_{\text{tip}}(t, \omega)$ .

The first  $N_s = 3$  sampled time series of the lift  $L_i(t, \omega)$  of the UASFE discretization with



(a) lift samples  $L_i(t)$  (b) lift response surface  $L(t, \omega)$  at  $t = 1$   
Figure 7: Results for the AGARD 445.6 wing with random free stream velocity  $U_\infty(\omega)$ .

$N_e = 1$  element show in Figure 7a that the first bending mode is the dominant mode in the system response. A second mode which is initially present in the response, damps out quickly, such that a wavelet decomposition pre-processing step is in this case not necessary to obtain the stochastic solution using UASFÉ. The samples illustrate that the free stream velocity has a significant effect on the frequency and the damping of the system response, which results in a diverging oscillation for  $i = 3$ , and decaying oscillations for  $i = 1$  and mean value  $\mu_{U_\infty}$  at  $i = 2$ . The same conclusions can be drawn from Figure 7b in which the response surface approximation of the lift  $L(t, \omega)$  at  $t = 1$  is given for  $N_e = 5$  elements and  $N_s = 11$  samples. The response surface has an oscillatory character due to the effect of the random  $U_\infty(\omega)$  on the frequency of the lift oscillation and consequently on the phase differences in  $L(t, \omega)$  at  $t = 1$ . The adaptive UASFÉ grid refinement results automatically in a gradually finer mesh in the region of large lift amplitudes at large values of  $U_\infty(\omega)$ .

Results for the time evolution of the mean  $\mu_L(t)$  and the standard deviation  $\sigma_L(t)$  of the lift are given in Figure 8 for  $N_e = 4$  and  $N_e = 5$  elements. The two approximations are converged with respect to each other up to  $5 \cdot 10^{-3}$ . The time history for the mean lift  $\mu_L(t)$  shows a decaying oscillation up to  $t = 0.4$ s from the initial value of  $\mu_L = -23.9$ N. This behavior can be explained by the decaying lift oscillation for a large range of  $U_\infty(\omega)$  values and the effect of  $U_\infty(\omega)$  on the increasing phase differences with time. For  $t > 0.4$  the decay is approximately balanced by the exponentially increasing amplitude of the unstable part of the  $U_\infty(\omega)$  parameter domain. In contrast, the standard deviation shows an oscillatory increase from the initial  $\sigma_L = 2.46$ N up to a local maximum of  $\sigma_L = 18.3$ N at  $t = 0.31$ s due to the increasing phase differences with time. For  $t > 0.31$  the standard deviation slightly decreases due to the decreasing lift amplitude in part of the parameter domain. Eventually, the unstable realizations result in an increasing standard deviation which reaches at  $t = 1$  values between  $\sigma_L = 14$  and  $\sigma_L = 19$ , which corresponds to an amplification of the initial standard deviation with a factor 6 to 8.

The nodal description of the structure directly returns the vertical tip-node displacement  $y_{tip}(t, \omega)$ . The approximations of the mean  $\mu_{y_{tip}}(t)$  and standard deviation  $\sigma_{y_{tip}}(t)$  of  $y_{tip}(t, \omega)$  show in Figure 9 a qualitatively similar behavior as the lift  $L(t, \omega)$ . The standard deviation  $\sigma_{y_{tip}}(t)$  vanishes, however, initially due to the deterministic initial condition for the structure in contrast with the non-zero  $\sigma_L(t)$  at  $t = 0$ . The standard deviation reaches values between  $\sigma_{y_{tip}} = 4.2 \cdot 10^{-3}$ m and  $\sigma_{y_{tip}} = 5.6 \cdot 10^{-3}$ m at  $t = 1$ , which corresponds

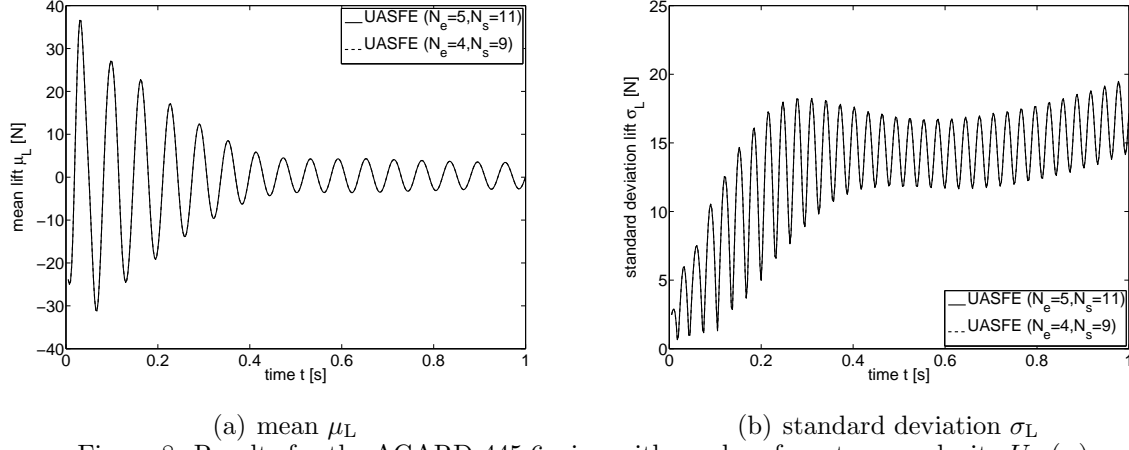


Figure 8: Results for the AGARD 445.6 wing with random free stream velocity  $U_\infty(\omega)$ .

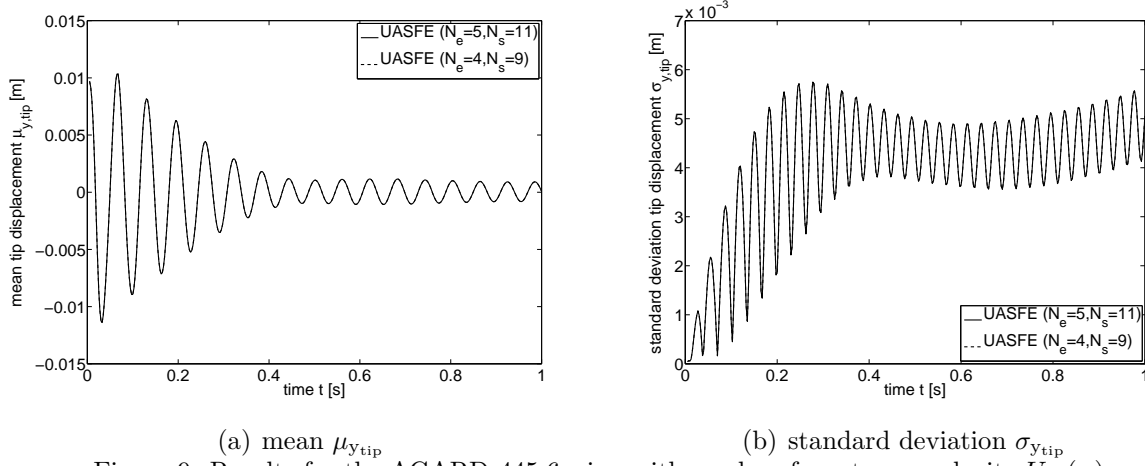


Figure 9: Results for the AGARD 445.6 wing with random free stream velocity  $U_\infty(\omega)$ .

to a standard deviation equal to 42% and 56% of the deterministic initial vertical tip deflection.

The probability of flutter can be determined by constructing the probability distribution of the damping factor of the system given in Figure 10. The damping factor is here extracted from the last period of oscillation of the sampled vertical tip node displacements. Positive and negative damping factors denote unstable and damped oscillatory responses, respectively. Even though the mean free stream velocity  $\mu_{U_\infty}$  is fixed at a safety margin of 5% below the deterministic flutter velocity  $U_{flut}$ , the non-zero probability of positive damping indicates a non-zero flutter probability. The 3.5% variation in  $U_\infty(\omega)$  results actually in a probability of flutter of 6.19%. Taking physical uncertainties into account in numerical predictions is, therefore, a more reliable approach than using safety margins in combination with deterministic simulation results.

## 6 CONCLUSIONS

An uncertainty quantification formulation for achieving a constant accuracy in time with a constant number of samples in multi-physics aeroelastic problems is developed based on interpolation of oscillatory samples at constant phase instead of at constant time.

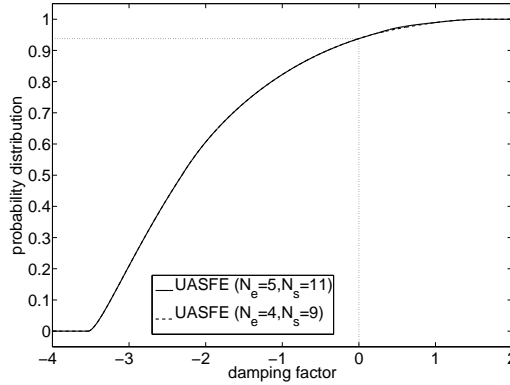


Figure 10: Results for the AGARD 445.6 wing with random free stream velocity  $U_\infty(\omega)$ .

The scaling of the samples with their phase eliminates the effect of the increasing phase differences in the response, which usually leads to the fast increasing number of samples with time. The resulting formulation is not subject to a parameterization error and it can resolve time-dependent functionals that occur for example in transient behavior. Phase-scaled uncertainty quantification results in a bounded error as function of the phase for periodic responses and under certain conditions also in a bounded error in time. The developed approach is applied to the unsteady fluid-structure interaction test cases of a two-dimensional airfoil flutter problem and the three-dimensional aeroelastic AGARD 445.6 wing.

In the stochastic post-flutter analysis of a two-degree-of-freedom rigid airfoil in Euler flow with nonlinear structural stiffness in pitch and plunge, a combination of randomness in two system parameters is considered. The behavior of the mean, standard deviation, and response surface of the angle of attack is resolved as indicator for the post-flutter airfoil behavior. The asymptotic stochastic behavior of the time-dependent problem is steady with a standard deviation of 1.6 degrees, which is a factor 16 larger than the deterministic initial angle of attack. Convergence results for discretizations with increasing number of samples indicate that the applied uncertainty quantification methodology results in practice in a time-independent accuracy with a constant number of samples.

For the AGARD aeroelastic wing configuration the effect of randomness in the free stream velocity is studied. Even though the mean free stream velocity is fixed at a safety margin of 5% below the deterministic flutter velocity, a 3.5% coefficient of variation results in a non-zero flutter probability of 6.19%. Taking physical uncertainties into account in numerical predictions is, therefore, a more reliable approach than using safety margins in combination with deterministic simulation results.

## 7 REFERENCES

- [1] Babuška, I., Tempone, R., Zouraris, G.E. (2004). Galerkin finite element approximations of stochastic elliptic partial differential equations. *SIAM J. Numer. Anal.*, 42, 800–825.
- [2] Babuška, I., Nobile, F., Tempone, R. (2007). A stochastic collocation method for elliptic partial differential equations with random input data. *SIAM J. Numer. Anal.*, 45, 1005–1034.

- [3] Ghanem, R.G., Spanos, P. (1991). *Stochastic finite elements: a spectral approach*. Springer-Verlag, New York.
- [4] Hosder, S., Walters, R.W., Perez, R. (2006). A non-intrusive polynomial chaos method for uncertainty propagation in CFD simulations. AIAA-2006-891, 44th AIAA Aerospace Sciences Meeting and Exhibit, Reno, Nevada.
- [5] Loeven, G.J.A., Bijl, H. (2008). Probabilistic collocation used in a two-step approach for efficient uncertainty quantification in computational fluid dynamics. *CMES*, 36, 193–212.
- [6] Mathelin, L., Hussaini, M.Y., Zang, Th.A. (2005). Stochastic approaches to uncertainty quantification in CFD simulations. *Num. Alg.*, 38, 209–236.
- [7] Reagan, M.T., Najm, H.N. Ghanem, R.G., Knio, O.M. (2003). Uncertainty quantification in reacting-flow simulations through non-intrusive spectral projection. *Combust. Flame*, 132, 545–555.
- [8] Witteveen, J.A.S., Bijl, H. (2008). A monomial chaos approach for efficient uncertainty quantification in nonlinear problems. *SIAM J. Sci. Comput.*, 30, 1296–1317.
- [9] Witteveen, J.A.S., Bijl, H. (2008). Efficient quantification of the effect of uncertainties in advection-diffusion problems using polynomial chaos. *Numer. Heat Tr. B-Fund.*, 53, 437–465.
- [10] Xiu, D., Karniadakis, G.E. (2002). The Wiener-Askey polynomial chaos for stochastic differential equations. *SIAM J. Sci. Comput.*, 24, 619–644.
- [11] Pettit, C.L., Beran, P.S. (2006). Spectral and multiresolution Wiener expansions of oscillatory stochastic processes. *J. Sound Vib.*, 294, 752–779.
- [12] Witteveen, J.A.S., Loeven, G.J.A., Sarkar, S., Bijl, H. (2008). Probabilistic collocation for period-1 limit cycle oscillations. *J. Sound Vib.*, 311, 421–439.
- [13] Witteveen, J.A.S., Bijl, H. (2008). An unsteady adaptive stochastic finite elements formulation for rigid-body fluid-structure interaction. *Comput. Struct.*, 86, 2123–2140.
- [14] Witteveen, J.A.S., Bijl, H. (2008). An alternative unsteady adaptive stochastic finite elements formulation based on interpolation at constant phase. *Comput. Method Appl. M.*, 198, 578–591.
- [15] Witteveen, J.A.S., Bijl, H. (2009). A TVD uncertainty quantification method with bounded error applied to transonic airfoil flutter. *Commun. Comput. Phys.*, 6, 406–432.
- [16] Witteveen, J.A.S., Loeven, G.J.A., Bijl, H. (2009). An adaptive stochastic finite elements approach based on Newton-Cotes quadrature in simplex elements. *Comput. Fluids*, 38, 1270–1288.
- [17] Witteveen, J.A.S., Bijl, H. (2009). Effect of randomness on multi-frequency aeroelastic responses resolved by unsteady adaptive stochastic finite elements. *J. Comput. Phys.*, submitted.

- [18] Sarkar, S., Witteveen, J.A.S., Loeven, G.J.A., Bijl, H. (2009). Effect of uncertainty on the bifurcation behavior of pitching airfoil stall flutter. *J. Fluid Struct.*, 25, 304–320.
- [19] Witteveen, J.A.S., Sarkar, S., Bijl, H. (2007). Modeling physical uncertainties in dynamic stall induced fluid-structure interaction of turbine blades using arbitrary polynomial chaos. *Comput. Struct.*, 85, 866–878.
- [20] Witteveen, J.A.S., Bijl, H. (2009). Higher period stochastic bifurcation of nonlinear airfoil fluid-structure interaction. *Math. Probl. Eng.*, in press.
- [21] Melchers, R.E. (1987). *Structural reliability: analysis and prediction*. Wiley, New York.
- [22] Fung, Y. (1969). *An introduction to aeroelasticity*. Dover Publications, New York.
- [23] Lee, B.H.K., Jiang, L.Y., Wong, Y.S. (1998). Flutter of an airfoil with a cubic non-linear restoring force. AIAA-1998-1725, 39th AIAA/ASME/ASCE/AHS/ASC Structures, Structural Dynamics, and Materials Conference, Long Beach, California.
- [24] De Boer, A., Van der Schoot, M.S., Bijl, H. (2007). Mesh deformation based on radial basis function interpolation. *Comput. Struct.*, 85, 784–795.
- [25] Yates Jr., E. (1987). AGARD standard aeroelastic configurations for dynamic response. Candidate configuration I.-Wing 445.6. Technical Memorandum 100492, NASA.
- [26] Openfem (2006). A finite element toolbox for Matlab and Scilab. Available on: <http://www-rocq.inria.fr/OpenFEM/>, release 2006a.
- [27] Van Zuijlen, A.H., De Boer, A., Bijl, H. (2007). Higher-order time integration through smooth mesh deformation for 3D fluid-structure interaction simulations. *J. Comput. Phys.*, 224, 414–430.
- [28] Beaubien, R., Nitzsche, F., Feszty, D. (2005). Time and frequency domain solutions for the AGARD 445 wing. International Forum on Aeroelasticity and Structural Dynamics (IFASD), Munich, Germany.
- [29] Chorin, A.J., Marsden, J.E. (1979). *A mathematical introduction to fluid mechanics*. Springer-Verlag, New York.
- [30] Kennedy, C., Carpenter, M. (2003). Additive Runge-Kutta schemes for convection-diffusion-reaction equations. *Appl. Numer. Math.*, 44, 139–181.
- [31] Van Zuijlen, A.H., Bijl, H. (2005). Implicit and explicit higher-order time integration schemes for structural dynamics and fluid-structure interaction computations. *Comput. Struct.*, 83, 93–105.
- [32] Van Zuijlen, A.H., Bijl, H. (2006). Implicit and explicit higher-order time integration schemes for fluid-structure interaction computations. *Int. J. Multiscale Comput. Eng.*, 4, 255–263.
- [33] Koobus, B., Farhat, C. (1999). Second-order time-accurate and geometrically conservative implicit schemes for flow computations on unstructured dynamic meshes. *Comput. Methods Appl. Mech. Engrg.*, 170, 103–129.